A Satellite Technique for Quantitatively Mapping Rainfall Rates over the Oceans

T. T. WILHEIT AND A. T. C. CHANG

Goddard Space Flight Center, Greenbelt, Md. 20771

M. S. V. RAO[1]

Environmental Research and Technology, Inc., Concord, Mass. 01742

E. B. RODGERS AND J. S. THEON

Goddard Space Flight Center, Greenbelt, Md. 20771

(Manuscript received 12 June 1975, in revised form 1 February 1977)

ABSTRACT

A theoretical model for calculating microwave radiative transfer in raining atmospheres is developed. These calculations are compared with microwave brightness temperatures at a wavelength of 1.55 cm measured by the Electrically Scanning Microwave Radiometer (ESMR) on the Nimbus 5 satellite and rain rates derived from WSR-57 meteorological radar measurements. A specially designed ground-based verification experiment was also performed, wherein upward viewing microwave brightness temperature measurements at wavelengths of 1.55 and 0.81 cm were compared with directly measured rain rates. It is shown that over ocean areas, brightness temperature measurements from ESMR may be interpreted in terms of rain rate with about an accuracy of a factor of 2 over the range 1–25 mm h^{-1} rain rate.

1. Introduction

Since man's survival virtually depends upon favorable rainfall for the production of food, rainfall is one of the most widely observed meteorological parameters. Dating from the time of the earliest weather records, the measurement of rainfall over land surfaces has been a primary meteorological observation since this measurement requires only simple instrumentation. However, rainfall can be a sharply discontinuous process so that the rainfall measured at a point in space may not necessarily be representative of the larger scale rainfall pattern.

Perhaps even more important is the fact that the rainfall occurring over the oceans, which cover three-fourths of the earth's surface, is very poorly known. Ship observations, as is well known, are unsatisfactory due to platform instability and sea-spray problems. Island reports are not representative of the surrounding ocean because 1) there are vast oceanic areas where there are few islands and 2) even in regions with a fair number of islands, orographic effects modify the flow and rainfall patterns, especially in the tropics.

Radar has provided much insight into the complex nature of rainfall structure and variability. The advantage of radar, unlike the point measurements of a raingage network, results from its ability to sense a volume of the atmosphere and translate this into rainfall rates over a given location. However, in normal practice, problems with attenuation and calibration limit the accuracy of radar for the determination of rainfall, and its fixed location and limited coverage make it unsuitable for global-scale measurements over the oceans. Thus, our knowledge of the total global rainfall and the water budget of the atmosphere is extremely limited. Whether the total rainfall under normal, drought and wet years for a given geographical region is merely the result of redistribution of the rainfall, or the result of fluctuations in the global rainfall, or both, has been impossible to determine.

Many ingenious schemes for indirect estimation of rainfall have been devised, some of which may be mentioned. Barrett (1970) worked out a rainfall coefficient based on cloud cover and cloud type. Another approach that has been developed relies upon the relationship between the reflected solar brightness of satellite pictures and rainfall rates. Martin and Suomi (1972) found that brightness regions correlate well with large radar echoes. An infrared technique was developed by Scherer and Hudlow (1971) wherein cloud heights and areas are derived from High Resolution Infrared Radiometer (HRIR) data and are used to estimate precipitation, cirrus contamination being

[1] Present affiliation: Systems and Applied Sciences Corp., Riverdale, Md. 20840.

ignored. Another indirect method adopted by Tucker (1961), and followed by Reed and Elliott (1973) to estimate precipitation in the northern Pacific, involves developing quantitative relations between current weather (ww) and rainfall amounts (RR) in the present weather reports from land stations and extending these relations to infer rainfall from ship weather reports.

The Electrically Scanning Microwave Radiometer (ESMR) system provides a more nearly direct approach. The greatest advantage of the system (which will be outlined in brief presently) is its selective response to liquid water. Although admittedly there are certain limitations, ESMR seems to be a better tool than any other available at present.

2. The ESMR system

The ESMR System carried on Nimbus 5 (Wilheit, 1972; Wilheit *et al.*, 1973) receives radiation emitted by the earth and its atmosphere in a 250 MHz bandwidth centered at 19.35 GHz. The antenna beam scans perpendicular to the direction of satellite motion in an arc of 100° every 4 s, the resolution being a 25 km circle near nadir degrading to an oval 45 km downtrack $\times$160 km cross track at the ends of the scan. The brightness temperature as observed from the satellite is dependent upon the emission from the earth's surface modified by the intervening atmosphere. The emissivity, being a function of the dielectric constant, is variable over land surfaces (depending on vegetation, soil type, etc.) and generally large ($\sim$0.9), but over oceans, the emissivity is more or less uniform at the ESMR wavelength (1.55 cm) and has a low value ($\sim$0.4). Furthermore, at this wavelength, the emissivity of water (ϵ_w) varies almost inversely as its thermodynamic temperature (T_w), with the result that the brightness temperature ($\epsilon_w T_w$) of a smooth water surface is virtually independent of temperature. Salinity has no consequential effect on the 1.55 cm radiance from the surface of the ocean. The wind at the surface of the ocean does affect the emissivity (Nordberg *et al.*, 1971; Hollinger, 1971). However, this effect is not strong enough to be a significant source of error in the present context.

It has been shown that the ESMR data may be qualitatively interpreted as indicating the presence or absence of rain above an unspecified threshold intensity (Wilheit *et al.*, 1973), and that the rain rate could be at least crudely estimated (Allison *et al.*, 1974). This qualitative relationship between ESMR brightness temperature and rainfall has been exploited by Allison, *et al.* (1975) in a study of tropical cyclones. In the present paper, this relationship will be established on a quantitative basis, theoretically supported and independently confirmed.

The equation of radiative transfer (Chandrashekar, 1960) may be written

$$\frac{dT_B(\theta)}{dz}+\gamma_{\text{ext}}T_B(\theta)=\gamma_{\text{sca}}\int_0^{\pi} T_B(\theta_s)F(\theta,\theta_s)\times\sin\theta_s d\theta_s+\gamma_{\text{abs}}T(z) \quad (1)$$

for an axially symmetric distribution of the γ's and T, an axially symmetric scattering process, and using the Rayleigh-Jeans approximation. Here $T_B(\theta)$ is the radiance in the direction specified by the polar angle (θ) expressed as an equivalent blackbody temperature or brightness temperature. The coordinate z is distance along a ray path, θ_s the scattering angle, γ_{ext} the total attenuation due to scattering and absorption, γ_{sca} the scattering coefficient, and γ_{abs} the absorptivity; $F(\theta,\theta_s)$ is the angular distribution of the scattering integrated azimuthally and normalized such that

$$\int_0^{\pi} F(\theta,\theta_s)\sin\theta_s d\theta_s=1; \quad (2)$$

and $T(z)$ is the thermodynamic temperature of the absorbing medium. Physically, the first term on the left-hand side of (1) expresses the change in the radiance in a particular direction. The second term gives the contribution to this change due to both absorption and scattering away from the specified angle. The integral term on the right-hand side expresses the increase in radiance in the θ direction due to scattering from other angles, and the second term represents the thermal emission of the medium.

In an atmosphere with rain three constituents contribute significantly to the absorption: molecular oxygen, water vapor and liquid water droplets. At these frequencies ice crystals are essentially transparent. Water droplets are the sole source of scattering of microwave radiation considered here. The oxygen contribution consists of a large number of resonances between 0.6 and 0.4 cm which blend into a continuum at sea level pressures and a single isolated line $\lambda=2.5$ mm. The effect at the wavelengths considered here (1.55 and 0.8 cm.) is only about 10 K or less; the model used is that of Meeks and Lilley (1963) as modified by Lenoir (1968). The effect of water vapor is due to a weak resonance at 1.35 cm and a number of strong ones at 1.64 mm and shorter wavelengths. The model for the absorption coefficient of water vapor used here is that given by Staelin (1966).

The interaction of a dielectric sphere with a plane electromagnetic wave was first solved by Mie (1908), and was discussed in the context of clouds and raindrops by Gunn and East (1954). The extinction (absorption and scattering) cross section of a liquid water droplet is given by

$$\sigma_{\text{ext}}=-\frac{\lambda^2}{2\pi}\,\text{Re}\sum_{n=1}^{\infty}(2n+1)(a_n+b_n) \quad (3)$$

and the scattering cross section by

$$\sigma_{sca}=\frac{\lambda^2}{2\pi}\sum_{n=1}^{\infty}(2n+1)(|a_n|^2+|b_n|^2), \tag{4}$$

where the magnetic and electric 2^n pole coefficients a_n and b_n are from expressions given by Stratton (1956) using the dielectric data of Lane and Saxton (1952). The angular distribution of amplitude of the scattered electromagnetic radiation is the sum of the radiation from the magnetic and electric 2^n poles. In the limit of small droplets, of radius less than about 100 μm for the frequencies considered here, only the electric dipole term b_1 need be considered. In this case the scattering is insignificant and the extinction cross section, which is then equivalent to the absorption cross section, reduces to

$$\sigma_{abs}=\sigma_{ext}=\frac{8\pi^2\rho^3}{\lambda}\,\mathrm{Im}\left(\frac{1-k}{2+k}\right), \tag{5}$$

where ρ is the radius of the droplet and k is the dielectric constant of water at the appropriate frequency. The absorption cross section is thus proportional to the volume of the droplet. The absorptivity can be related to the absorption cross section of a single droplet by

$$\gamma_{abs}=\int N(\rho)\sigma_{abs}(\rho)d\rho, \tag{6}$$

where $N(\rho)$ is the number density per unit size interval of droplets of radius ρ. Thus, the absorptivity is proportional to the mass density of the water droplet distribution, independent of the droplet size distribution as long as there are no particles with radius $\gtrsim 100$ μm. This condition is quite valid for nonraining clouds. The distribution of precipitating particles in a rainstorm is given by the Marshall–Palmer distribution

$$N(\rho)=N_0e^{-\Lambda\rho}, \tag{7}$$

where $N(\rho)$ is the number density of particles per unit size interval, ρ is in cm, the proportionality constant N_0 has the value 0.16 cm^{-4} for any intensity of rainfall and

$$\Lambda=81.56R^{-0.21}, \tag{8}$$

where R in the nominal rain rate (mm h^{-1}). This distribution was derived from physical measurements on raindrops at the surface and has been found to predict the radar returns from rain storms fairly well (Marshall, *et al.*, 1947; Marshall and Palmer, 1948).

An expression for the fall velocity of raindrops as a function of size is given by Waldteufel (1973) as

$$V(\rho)=965-1030\exp(-12\rho), \tag{9}$$

when V is the fall velocity (cm s^{-1}). The rain rate R for a given distribution of particle sizes may thus be calculated ignoring the vertical velocity of the air as

$$R'=\frac{4\pi}{3}\int V(\rho)\rho^3N(\rho)d\rho. \tag{10}$$

The rain rates so calculated will be referred to as computed rain rate and the rain rate R used as a parameter to specify a drop size distribution will be referred to as a nominal rain rate. Computed rain rates will be used for comparing theoretical calculations with experimental results. For small radii ($\rho<0.0054$ cm) the velocity given by (9) is negative; thus the lower limit of integration in (10) should be 0.0054 cm, otherwise small particles would contribute a negative rain rate.

The fall velocity given in (9) is valid for sea level pressure only; at higher altitudes the drag on the particles is less so the fall velocity is greater. According to Foote and duToit (1969) the fall velocity for a given size droplet is very nearly proportional to $D^{-0.4}$, where D is the local atmospheric density. For the present calculations we have scaled the drop size distribution with altitude (and thus with density) so that the computed rain rate is independent of altitude.

When the scattering and extinction cross sections, with dielectric properties appropriate for a wavelength of 1.55 cm and a temperature of 273 K, are numerically integrated over the Marshall-Palmer distribution, the

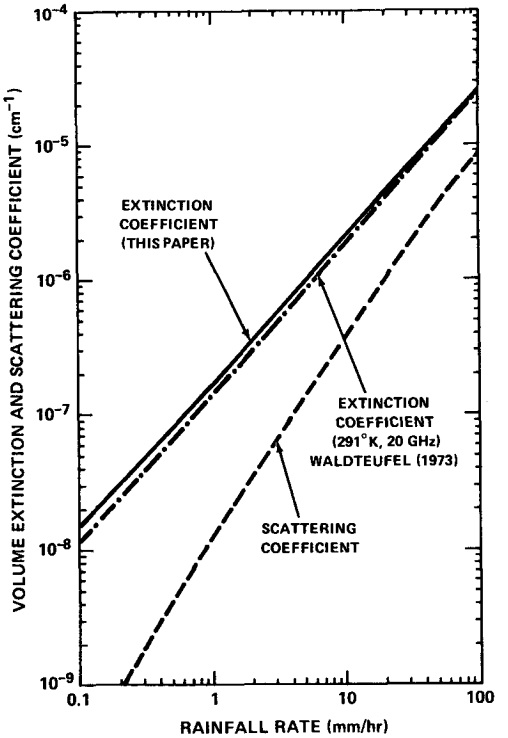

FIG. 1. Volume scattering coefficient and volume extinction coefficient at $\lambda=1.55$ cm for a Marshall-Palmer distribution of raindrops at the indicated rain rate for an assumed temperature of 273 K. [The results of Waldteufel (1973) for $\lambda=1.5$ cm and 291 K are shown for comparison.]

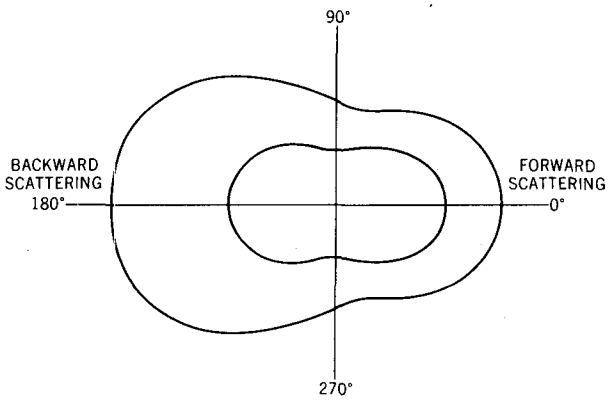

FIG. 2. Relative, azimuthally averaged, angular distribution of scattering of 1.55 cm radiation by a Marshall-Palmer distribution of raindrops at 1 mm h^{-1} (inner curve) and 25 mm h^{-1} (outer curve). The two curves are not to the same scale.

coefficients of extinction and scattering shown in Fig. 1 result. These calculations were also performed for a temperature of 293 K and the results were within 10% at all rain rates. Similar calculations were performed by Waldteufel (1973) for a wide range of wavelengths. His most nearly comparable case (1.5 cm, 291 K) is also given in Fig. 1. In Fig. 2 the azimuthally averaged relative angular distributions of the scattering are shown for nominal rain rates of 1 and 25 mm h^{-1}. In the low rain rate case, the droplets scatter like electrig dipoles oriented in the direction of the incoming electric field vector; thus the forward and backward scatterinc components are roughly equal and twice as large as the scattering perpendicular to the direction of incidence. In the 25 mm h^{-1} case, the larger particle size permits other multipole components to contribute, and the backward scattering is much larger than the forward scattering due primarily to interference between the electric and magnetic dipole components.

For purposes of calculation, the atmosphere is divided into many optically thin layers. A modified Marshall-Palmer distribution of raindrops as described is assumed from the freezing level to the surface. The relative humidity is assumed to vary linearly from 80% at the surface to 100% at the freezing level. Since the Marshall-Palmer distribution does not include cloud water droplets, a cloud with a net density of 25 mg cm^{-2} is distributed through the 0.5 km beneath the freezing level. This is quite similar to a model proposed by Kessler and Atlas (1959). They give an approximately constant rainwater content from the surface to a point near the freezing level. They suggest much larger water content above this, but primarily in the form of ice which has no consequential effect on the brightness temperature. They also include a nonraining cloud component, concentrated primarily just below the freezing level with a liquid water content varying from 20–40 mg cm^{-2} for rain rates between 2 and 20 mm h^{-1}. The ocean surface is assumed to have the reflectivity given by the Fresnel relations (Jackson 1962), based on the Lane and Saxton (1952) dielectric data. A lapse rate of 6.5°C km^{-1} is assumed and the surface temperature (or equivalently, freezing level) is adjusted as a parameter of the calculation. Above the freezing level, the relative humidity given by the 1962 U. S. Standard Atmosphere for that altitude is assumed. Water droplets are described by the Lane and Saxton (1952) dielectric data. The angular distribution of reflection from the ocean surface is assumed to be Lambertian (Born and Wolf, 1975).

Using this model, the upwelling and downwelling brightness temperatures are then computed, first ignoring the scattering so that the brightness temperatures

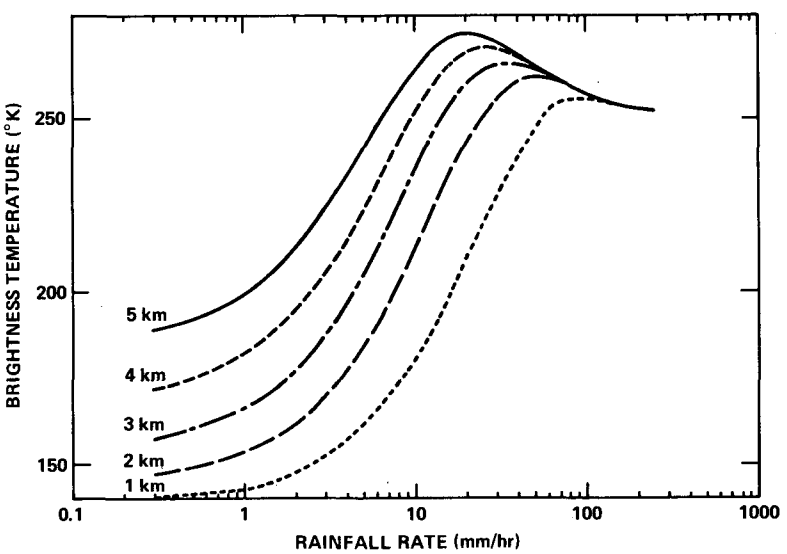

FIG. 3. Calculated brightness temperature at 1.55 cm as a function of rain rate for freezing levels of 1–5 km.

may be computed for a number of angles independently. The brightness temperatures are then recomputed iteratively using the brightness temperatures of the previous iteration for the scattering term until satisfactory convergence (to better than 0.1 K) is obtained.

Brightness temperatures for a set of five atmospheres and a range of rainfall rates were calculated for a wavelength of 1.55 cm. The surface temperatures were 279.6, 286.1, 292.6, 299.1 and 305.6 K, giving freezing levels of 1, 2, 3, 4 and 5 km, respectively. The Marshall-Palmer distribution of rain particles appropriate to each rain rate was assumed from the freezing level to the surface and scaled according to density as discussed. The results of this calculation are shown in Fig. 3. Note that there is no consequential effect of rain at rates <1 mm h^{-1}, but above that, the brightness temperature increases sharply with increasing rain rate to a maximum between $\sim$20–50 mm h^{-1} rain rate. At higher rain rates, the very strong backscattering of the larger droplets actually decreases the brightness temperature. The dependence on freezing level is about 50% in rain rate per kilometer change in the freezing level at a given brightness temperature.

To demonstrate the effect of scattering, the brightness temperatures were calculated for the 4 km freezing level case with the scattering term artificially suppressed in the calculation. The results of this calculation are compared to the full calculation in Fig. 4. Up to 10 mm h^{-1} there is little effect due to the scattering, but above this value the effect is to lower the brightness temperature significantly. This calculation also permits further insight into the relationship between brightness temperature and rain rate. The brightness temperature is determined primarily by the absorption with the scattering serving as a relatively small correction. Both the absorption coefficient and the rain rate have been expressed as integrals over the drop size distribution. Both rain rate and absorption coefficient can thus be expressed in the form

$$P_j = \int_0^\infty F_j(\rho) G(\rho) d\rho,$$

where $G(\rho) = \rho^3 N(\rho)$ and $F_j(\rho)$ is the remainder of the integrand for the desired parameter P_j. In Fig. 5, we show $G(\rho)$ for a 10 mm h^{-1} rain rate Marshall-Palmer distribution, $F_{ABS}(\rho)$ for 1.55 cm and 273 K, and $F_{RR}(\rho)$ based on the above given fall velocity. It can be seen that the rain rate and absorption coefficient represent similar moments of the particle size distribution. Thus, although both the brightness temperature and rain rate are individually dependent on the drop size distribution, the relationship between the two should not be excessively dependent on the details of the particle size distribution. As a test of this insensitivity to drop size distribution some numerical experiments were carried out. The first was to replace the Marshall-Palmer distribution with the Sekhon-Srivastava (1971) distribution; the brightness temperature curve resulting from this change is indicated on Fig. 4. There is no change in the brightness expected for rain rates <20 mm h^{-1}. Above this the brightness temperature is determined primarily by the balance between scattering and absorption and the paucity of large particles in the

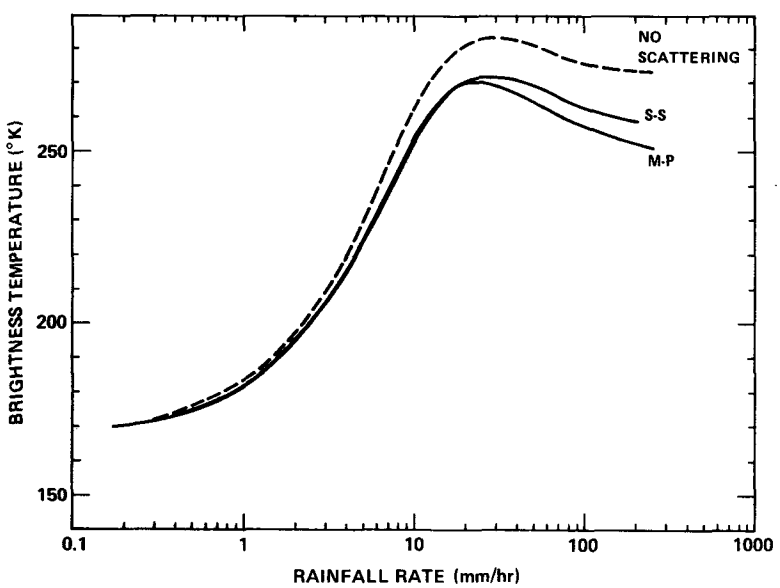

FIG. 4. Calculated brightness temperature at 1.55 cm as a function of rain rate with scattering included in the model (solid lines) and excluded from the model (dashed line). In both cases, the assumed freezing level is 4 km. The M-P and S-S designations specify the Marshall-Palmer and Sekhon-Srivastava particle size distributions, respectively.

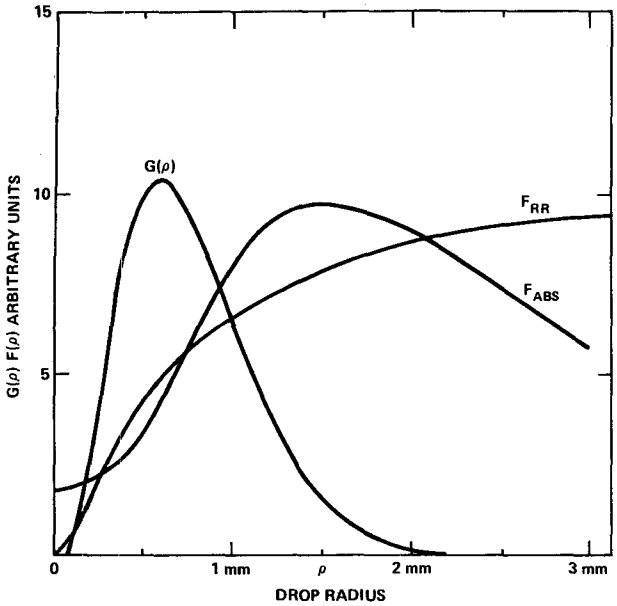

FIG. 5. Components of integrand for rain rate and for absorption coefficient at a wavelength of 1.55 cm and for a rain rate of 10 mm h^{-1}.

Sekhon-Srivastava distribution at large rain rates favors absorption over scattering.

It has been noted by many authors, of whom Sander (1975) is a recent example, that an exponential distribution function such as Marshall-Palmer overestimates the number of very small particles. To test the sensitivity of our model to this, we imposed a minimum radius of 0.05 cm and recalculated the brightness temperature/rain rate relationships. The difference was found to be less than 0.5 K. Similarly, Walker *et al.* (1964) found that imposing a maximum radius of $0.115R^{0.213}$ [cm] on the Marshall-Palmer distribution improved the agreement with radar data but our model is found not be be sensitive to this change.

3. Nimbus 5 observations

The confirm this theoretical model, simultaneous measurements of rain rate and microwave brightness temperature over ocean areas were needed. Four cases were found where data were taken by the WSR-57 meteorological radar at Miami, Fla., coincident with Nimbus 5 overpasses (to within 5 min). The dates and times of these are given in Table 1. In all cases, a tropical maritime atmosphere with the freezing level at 4 km was assumed.

The WSR-57 meteorological radar measures the backscattered microwave signal at a wavelength of 10.3 cm (2.91 GHz). The range resolution is 1.2 km out to a maximum of 200 km. The azimuthal resolution is 2°. The return signal in each range-azimuth bin is digitally converted to rain rate through a statistically derived relationship; this rain rate is expressed in tenths of millimeters per hour. Further description of the WSR-57 radar and the means by which radar return may be interpreted as rain rate can be found in Wiggert and Ostlund (1975).

In order to compare the data, the WSR-57 data were first plotted on a map base; the ESMR data were then overlaid using the image of the Florida coast line and Lake Okeechobee visible in the ESMR data as a guide to insure registration. Fig. 6 is an image of the WSR-57 data for the pass, where the crosses show the location of the beam centers for the corresponding ESMR data. The two ovals show the approximate 3 db (half-power) and 1.5 db antenna gain contours for a typical ESMR beam position. Since the ESMR resolution is much coarser than that of the WSR-57, the radar data must be averaged over the radiometer resolution element. To approximate the effect of the antenna pattern, the radar data within the 1.5 db gain contour were given full weight while those between the 1.5 and 3.0 db contours were given half weight in the averaging. Only those beam positions with centers more than 50 km from the coast and with scan angles $<40°$ were included. The greatest rain rate observed was 79 mm h^{-1} in the 25 June 1974 case. However, when averaged to the ESMR resolution, the maximum observed was 16.6 mm h^{-1}. In Fig. 7, the results of this comparison are shown as solid points. The solid line is the brightness temperature computed for the 4 km freezing level. The two dashed lines represent departures of the larger of a factor of 2 in rain rate or 1 mm h^{-1}. Note that virtually all the points are within or very near this envelope. The bulk of the departure of the observations from this envelope is to the lower brightness temperature side as would be expected for intense rain (≥ 20 mm h^{-1}) not filling the instantaneous field of view of the ESMR. The intense rain would contribute to the average rain rate over the field of view out of proportion to its contribution to the similarly averaged brightness temperature due to the saturation of the rain rate/brightness temperature relationship at large rain rates. The crosses are inferred from the ground-based measurements discussed in the next section.

4. Ground-based verification

As an independent verification of the theoretical model, two microwave radiometers with wavelengths of 1.55 and 0.8 cm were mounted viewing upward at a 45° zenith angle. The relevant parameters of each are

TABLE 1. Times and dates of the WSR-57 radar observations.

Date	Time
20 June 1973	1632 GMT
7 July 1973	1610 GMT
24 June 1974	1605 GMT
25 June 1974	1705 GMT

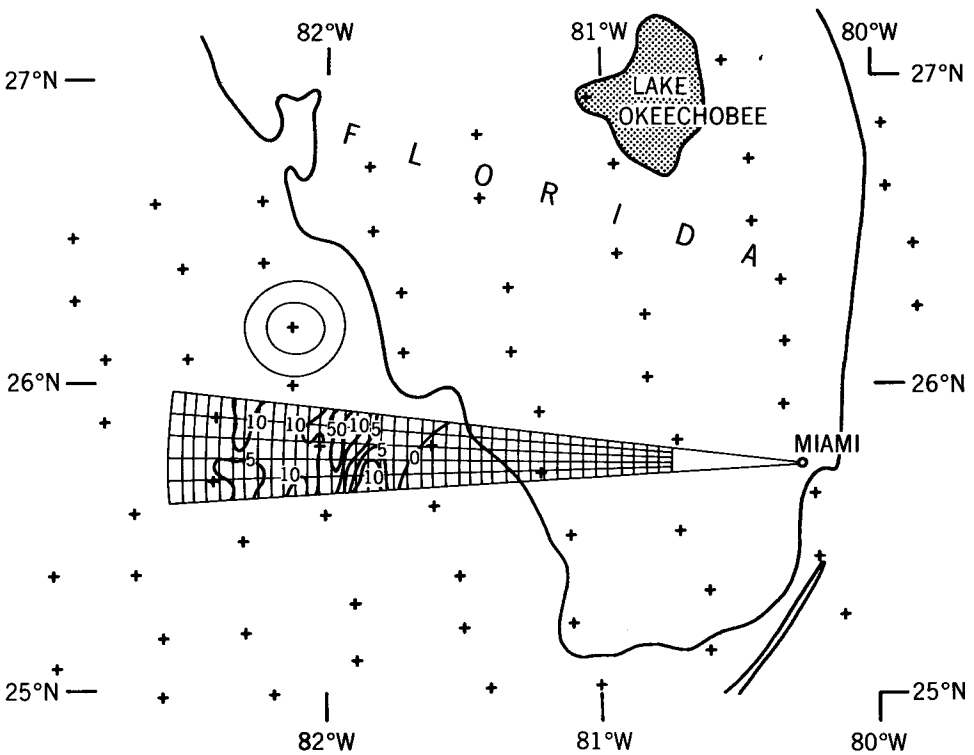

FIG. 6. A portion of the WSR-57 radar data for the 25 June 1973 case. The cross hatching shows the range and azimuth resolution of the radar. Isopleths of 0, 5, 10 and 50 mm h^{-1} rain rate are indicated. The crosses indicate the locations of the beam centers of the corresponding Nimubs 5 ESMR data. The 1.5 dB (inner oval) and 3 dB (outer oval) contours are shown for a typical ESMR beam position.

summarized in Table 2. The rectangular cross section, horn-type antennas were mounted with the electric field vector horizontal so that the *E*-plane antenna gain pattern, having larger sidelobes than the *H*-plane gain pattern, caused a minimum variation in elevation throughout the field of view. The antenna horns were shielded from direct rain by a wooden housing open on one side. They were protected against wetting from blowing rain by using a plastic wrapping across their apertures and a blower which directed a stream of dry air across the plastic wrap. The receivers were connected in turn for a period of 15 s each 1) to their respective antennas, 2) to a reference cold load and 3) to a reference warm load. The output from this radiometer system was fed to a small computer which calculated both of the mean brightness temperatures for the 15 s when the radiometers were sensing the radiation from the antennas (separately at 19.35 and 37.0 GHz) and printed out the results at intervals of 0.8 min.

TABLE 2. Radiometer parameters.

	Radiometer 1	Radiometer 2
Frequency	19.35 GHz	37.0 GHz
Wavelength	1.55 cm	0.81 cm
Bandwidth	400 MHz	400 MHz
E plane beamwidth	6.5 °	6.5°
H plane beamwidth	9.0°	9.0°

Two raingages of different types were used to measure the rainfall intensities simultaneously with the radiometer observations. The first was a conventional tipping bucket raingage located adjacent to the antenna housings. The number of times the bucket tipped was registered by a counter and recorded on the computer print-out alongside the radiometer readings. The second was the recently developed (Raymond and Wilson, 1974) electronic rain intensity gage with a 1 s response time, located at a horizontal distance of 23.5 m from the radiometers in the direction of the antenna beams. In this type of raingage, measurement is made of the ratio of the resistance of rainwater flowing in a trough between two electrodes spaced along the trough (R_1), to the resistance of the same rainwater in a chamber of fixed geometry (R_2). Since R_1 varies as the resistivity divided by the cross-sectional area of the flowing water, while R_2 varies only as the resistivity, R_2/R_1 is independent of resistivity and is proportional to the cross-section area, i.e., it is related only to the rate of flow. Both raingages were calibrated against directly measured flow rates and both had 91 cm funnel apertures.

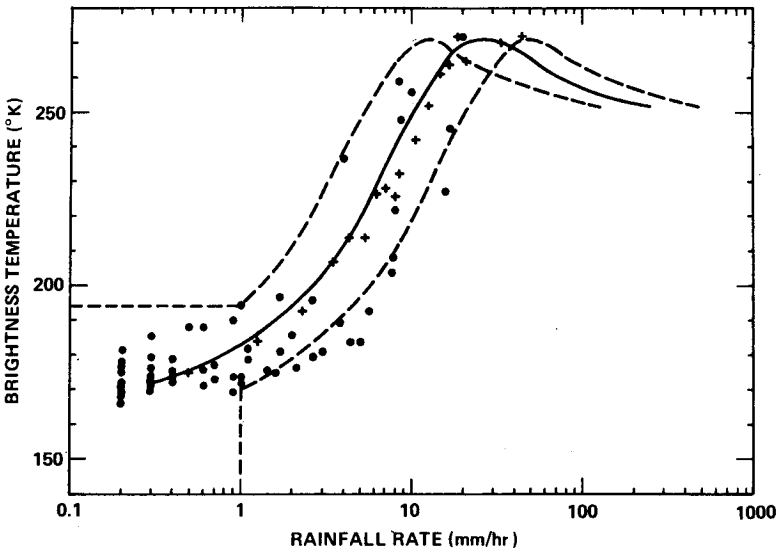

FIG. 7. Brightness temperature as a function of rain rate: Nimbus 5 ESMR vs WSR-57 radar (dots) and inferred from ground-based measurements of brightness temperature and direct measurements of rain rate (crosses). The solid line is the calculated brightness temperature for a 4 km freezing level. The dashed lines represent departure of 1 mm h^{-1} or a factor of 2 in rain rate (whichever is greater) from the calculated curve.

Data were collected with this arrangement from June–September, 1974, at Goddard Space Flight Center. On all occasions on which data were taken, the freezing level was 4 ± 0.5 km. With the aid of the laboratory calibration curve, the voltage records on chart paper were translated to rainfall rates. The brightness temperatures of the 1.55 and 0.8 cm radiometer systems were tabulated against rainfall intensities. For this purpose, only those occasions when the rain

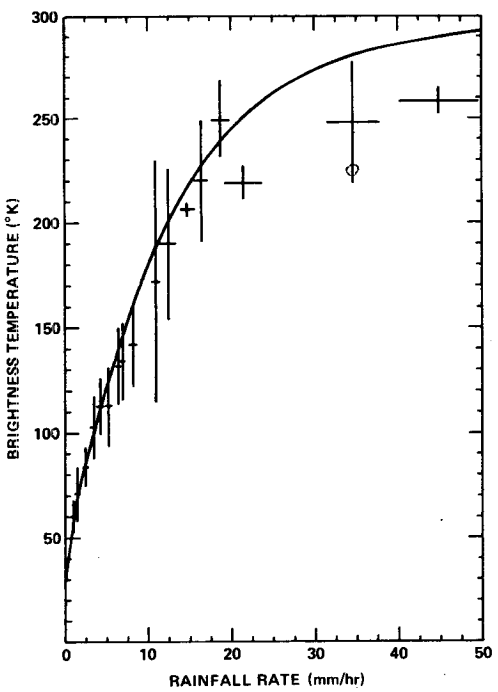

FIG. 8. Brightness temperature ($\lambda = 1.55$ cm) at viewing angle of 45° with respect to the zenith as a function of directly measured rain rate. At each point, the height and width of the cross represent two standard deviations in the corresponding dimensions. The solid line is the theoretically calculated curve.

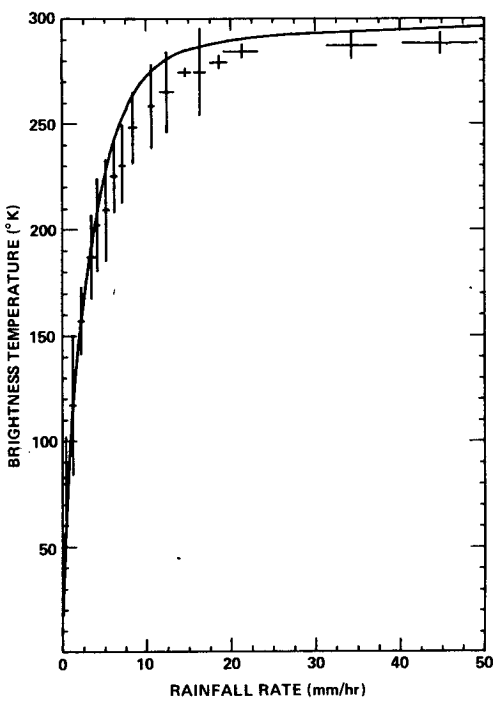

FIG. 9. As in Fig. 8 except at $\lambda = 0.81$ cm.

rate and temperatures were sensibly steady for 2 min or more were considered, in order to avoid excessive scatter in the data. The observations were then grouped under 18 categories according to rainfall rate intervals (ten categories at 1 mm h^{-1} intervals from 0–10 mm h^{-1}, five categories at 2 mm h^{-1} intervals from 10–20 mm h^{-1}, two categories at 10 mm h^{-1} intervals from 20–40 mm h^{-1}, and one category >40 mm h^{-1}). In each category the mean and standard deviation were calculated separately with respect to brightness temperature ($\bar{T}_B$ and σ_{TB}) and rainfall ($\bar{R}$ and σ_R). The diagram in Fig. 8 shows the result for 1.55 cm and the diagram in Fig. 9 those for 0.8 cm. In both diagrams, the vertical lines and horizontal lines are equal in length to two standard deviations. The solid curve, in each case, represents the corresponding theoretical calculation.

If one approximates the radiometric effect in this case by an isothermal, nonscattering layer of absorber at a temperature of 273 K, these upward viewing data can be converted to what would have been observed by the ESMR if this atmosphere were over water. These data are included in Fig. 7 and are quite consistent with the satellite observations and the theoretical calculations.

5. Conclusions

There are many weaknesses inherent to a study of this type. The most obvious is that there is much uncertainty in interpretation of radar returns in terms of rain rate. There is also some uncertainty in registering the ESMR data to the radar data; and having registered the two, it is not feasible to use an exact antenna pattern in averaging the rain rate over the instantaneous field of view of the ESMR. The nonlinearity of the rain rate/brightness temperature relationship reduces the validity of such an average still further. There are other variable factors which have been ignored; water vapor, wind speed and viewing angle, to name a few. All these factors contribute to the considerable scatter in the observed relationship between ESMR brightness and radar derived rain rates. Nevertheless, the data show clearly that in the dynamic range 1–20 mm h^{-1} rain rate, brightness temperature at 1.55 cm can be related to rain rate to within a factor of 2. Considering the difficulty of any rain rate measurement over an area, this is quite a useful measurement. The upward viewing data agree well with the theoretical model over a wide range of rain rates and at two different wavelengths (1.55 and 0.8 cm) so that by using this model, the microwave response to rain may be predicted for other wavelengths and viewing geometries. Since global data are now available from the Nimbus 5 ESMR, it is possible to measure the oceanic component of the atmospheric water budget.

Acknowledgments. The authors gratefully acknowledge the aid of Dr. W. L. Woodley and his co-workers at the Experimental Meteorological Laboratory, NOAA, Coral Gables, Fla., for the radar data; Dr. C. M. Fullerton of the Cloud Physics Laboratory, University of Hawaii, for the loan of the electronic raingage; Dr. R. J. Curran for the radiative transfer computer program; and Mr. R. E. Burbage for efforts much beyond his normal duties in operating the ground-based verification experiment.

REFERENCES

Allison, L., E. Rodgers, T. Wilheit and R. Wexler, 1975: A multisensor analysis of Nimbus 5 data on 22 January 1973. NASA-TN-D-7911, 43 pp.

——, ——, —— and R. Fett, 1974: Tropical cyclone rainfall as measured by the Nimbus 5 electrically scanning microwave radiometer. *Bull. Amer. Meteor. Soc.*, **55**, 1074–1089.

Barrett, E. C., 1970: The estimation of monthly rainfall from satellite data. *Mon. Wea. Rev.*, **98**, 322–327.

Born, M., and E. Wolf, *1975*: *Principles of Optics*. Pergamon Press, 182 pp.

Chandrashekar, S., 1960: *Radiative Transfer*. Dover, 393 pp.

Foote, C. B. and P. S. duToit, 1969: Terminal velocity of raindrops aloft. *J. Appl. Meteor.*, **8**, 249–253.

Gunn, K. L. S., and T. U. R. East, 1954: The microwave properties of precipitation particles. *Quart. J. Roy. Meteor. Soc.*, **80**, 522–545.

Hollinger, J. P., 1971: Passive microwave measurements of sea surface roughness. *IEEE. Trans. Geosci. Electr.*, **GE-9**, No. 3, 165–169.

Jackson, J. D., 1962: *Classical Electrodynamics*. Wiley, 216 pp.

Kessler, E., and D. Atlas, 1959: Model precipitation distributions. *Aerospace Eng.*, **18**, No. 12, 36–40.

Lane, J. A., and J. A. Saxton, 1952: Dielectric dispersion in pure polar liquids at very high radio frequencies. *Proc. Roy. Soc. London*, **A213**, 400–408.

Lenoir, W. B., 1968: Microwave spectrum of molecular oxygen in the mesosphere. *J. Geophys. Res.*, **73**, 361–376.

Marshall, T. S., R. C. Langille and W. McK. Palmer, 1947: Measurement of rainfall by radar. *J. Meteor.*, **4**, 186–192.

——, and W. McK. Palmer, 1948: The distribution of raindrops with size. *J. Meteor.*, **5**, 165–166.

Martin, D. W., and V. Soumi, 1972: A satellite study of cloud clusters over the tropical North Atlantic Ocean. *Bull. Amer. Meteor. Soc.*, **53**, 135–156.

Meeks, M. L., and A. Lilley, 1963: The microwave spectrum of oxygen in the earth's atmosphere. *J. Geophys. Res.*, **68**, 1683–1703.

Mie, G., 1908: Beiträge zur Optik trüber Medien, speziell kolloidaler Metallösungen. *Ann. Phys.*, **26**, 597–614.

Nordberg, W., J. Conway, D. Ross and T. Wilheit, 1971: Measurement of microwave emission from a foam-covered wind driven sea. *J. Atmos. Sci.*, **28**, 429–435.

Raymond, D. J., and K. Wilson, 1974: Development of a new rainfall intensity gauge. *J. Appl. Meteor.*, **13**, 180–182.

Reed, R. K., and W. P. Elliott, 1973: Precipitation at ocean weather stations in the North Pacific. *J. Geophys. Res.*, **78**, 7087–7091.

Sander, J., 1975: Experimental results with a rain analyzer. *J. Appl. Meteor.*, **14**, 128–131.

Scherer, W. D., and M. Hudlow, 1971: A technique for assessing probable distributions of tropical precipitation echo lengths for X-band radar from Nimbus 3 HRIR data. BOMEX Bull. No. 10, NOAA, 63–68.

Sekhon, R. S., and R. C. Srivastava, 1971: Doppler radar observations of drop-size distributions in a thunderstorm. *J. Atmos. Sci.*, **28**, 983–994.

Staelin, D. A., 1966: Measurements and interpretation of the

microwave spectrum of the terrestrial atmosphere near 1 centimeter wavelength. *J. Geophys. Res.*, **71**, 2875–2881.

Stratton, J. A., 1956: *Spheroidal Wave Functions, Including Tables of Separation Constants and Coefficients*. MIT Press.

Tucker, G. B., 1961: Precipitation over the North Atlantic Ocean. *Quart. J. Roy. Meteor. Soc.*, **87**, 147–158.

Waldteufel, P., 1973: Attenuation Des ondes hyperfrequences par la pluie: une mise au point. *Ann. Téléc.*, **28**, 255–272.

Walker, G. B., L. S. Lamberth and J. J. Stephens, 1964: Dual frequency radar observations of precipitation. *J. Appl. Meteor.*, **3**, 430–438.

Wiggert V., and Ostlund, S., 1975: Computerized rain assessment and tracking of south Florida weather radar echoes. *Bull. Amer. Meteor. Soc.*, **56**, 17–26.

Wilheit, T. J., 1972: The electrically scanning microwave radiometer (ESRM) experiment. *Nimbus 5 Users Guide*, NASA Goddard Space Flight Center, 55-105.

——, J. Theon, W. Shenk, L. Allison and E. Rodgers, 1973: Meteorological interpretations of the images from Nimbus 5 Electrically Scanning Microwave Radiometer. NASA X-651-73-189, 21 pp. [Also *J. Appl. Meteor.*, **15**, 168–172.]